Charles University in Prague
Faculty of Mathematics and Physics

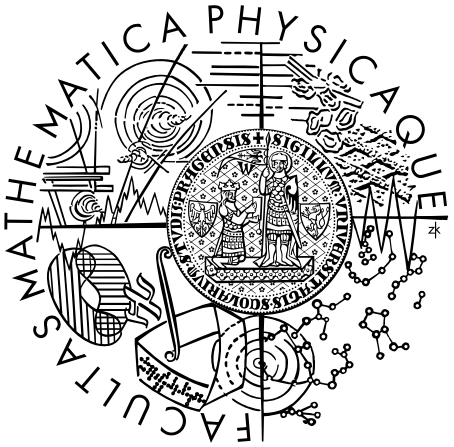

Abstract of Doctoral Thesis

Numerical modeling of present-day mantle convection

Nicola Tosi

Supervisor: Prof. Zdeněk Martinec

Prague, 2007

Univerzita Karlova v Praze
Matematicko-fyzikální fakulta

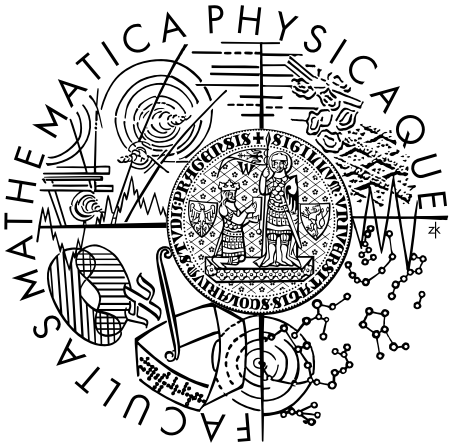

Autoreferát dizertační práce

Numerické modelování současné plášť'ové konvekce

Nicola Tosi

Školitel: Prof. Zdeněk Martinec

Praha, 2007

Dizertace byla vypracována na základě výsledků získaných v letech 2005–2007 během doktorandského studia na Katedře geofyziky MFF UK.

Dizertant:
Nicola Tosi
Katedra geofyziky MFF UK
V Holešovičkách 2, Praha 8, 180 00

GeoForschungsZentrum Potsdam
Telegrafenberg, 14473, Potsdam (Germany)

Školitel:
Prof. RNDr. Zdeněk Martinec
Katedra geofyziky MFF UK
V Holešovičkách 2, Praha 8, 180 00

Oponenti:
Mgr. Hana Čížková, Dr.
Katedra geofyziky MFF UK
V Holešovičkách 2, Praha 8, 180 00

Prof. Luce Fleitout
Laboratory of Geology, École Normale Supérieure
24 rue Lhomond, 75231 Paris Cedex 05 (France)

Prof. Giorgio Spada
Institute of Physics, University of Urbino
Via Santa Chiara 27, 61029 Urbino (Italy)

Předseda oborové rady:
Doc. RNDr. Oldřich Novotný, CSc.
Katedra geofyziky MFF UK
V Holešovičkách 2, Praha 8, 180 00

Autoreferát byl rezeslán dne

Obhajoba dizertace se koná dne v hodin před komisí pro obhajoby dizertačních prací v oboru F-7: Geofyzika v budově MFF UK, Ke Karlovu 3, Praha 2, v místnosti č. 105.

S dizertací je možno se seznámit v PGS MFF UK, Ke Karlovu 3, Praha 2.

Contents

Introduction **6**

1 Model equations and solution techniques **8**
1.1 Equations and boundary conditions 8
1.2 Matrix propagator technique 9
1.3 Spectral–finite element approach 11
1.4 Validation with 1D viscosity distributions 12

2 A semi-analytical solution for axisymmetric viscosity **15**
2.1 Outline of the solution 15
2.2 Comparison with the SFE solution 17

3 Low-degree geoid over subduction zones **20**
3.1 Model setting 20
3.2 Results and discussion 20

Conclusions **24**

References **25**

Introduction

Mantle convection is the mechanism accepted to explain the dynamics of the Earth's interior. To model mantle material that on geological time-scales flows like a viscous fluid, two complementary approaches can be adopted. On the one hand, one can solve self-consistently the equations of thermal convection, including parameters and employing physical relationships derived from mineral physics. On the other hand, to permit comparison with specific observables that are associated with the flow, one can consider a more restricted problem. Instead of focusing on the time evolution of mantle flow, if the density anomalies that drive the convection are known *a priori*, a snapshot of the *present-day* flow pattern can be built, that is consistent with these anomalies and that can successfully predict the observables. Our work is largely motivated by the latter approach.

Since the pioneering work of Pekeris (1935), several authors recognized the possibility of constraining mantle properties by modeling the *non-hydrostatic geoid* (e.g. Runcorn, 1967; Ricard et al., 1984). The density anomalies of thermal origin that are responsible for the mantle buoyancy can be retrieved through the seismic tomography (e.g. van der Hilst et al., 1997; Ritsema & van Heijst, 2000). Once the lateral density heterogeneities of the mantle are known, the geoid can be computed as the result of a static and a dynamic contribution. On one side, being the geoid a measure of the gravitational potential, the Newton's law can be used to integrate directly the density field delivered by seismic tomography. On the other side, the same anomalies can be used to compute the present-day mantle flow and the additional anomalies that arise at the Earth's surface and at the CMB as a consequence of the *dynamic topography* induced by the flow (see Fig. 1). It turns out that the static and dynamic contributions have similar amplitudes and opposite signs. The total geoid is then the result of these two different and opposing effects. Thus, even if we were completely sure about the distribution of the density heterogeneities, the geoid depends strongly upon the rheology of the mantle and a careful modeling of the mantle flow is necessary. To this purpose, the partial differential equations (PDE) that govern the dynamics of slow viscous flow (*Stokes problem*) must be solved.

To solve such equations, two approaches are considered. To treat problems with radially symmetric viscosity distributions, we implement the technique of the *matrix propagator* (Hager & Clayton, 1989), which, over the last twenty years, has been the principal mathematical tool upon which models of present-day mantle convection have been built. The matrix propagator, provides us with an analytical solution of the Stokes problem that is used to benchmark a more general algorithm. In fact, to treat problems that include lateral viscosity variations (LVV), no analytical solution exist and a strictly numerical approach becomes mandatory. Therefore, we develop and implement what we term the spectral finite element (SFE) method. After converting the classical differential form of the problem to an equivalent integral form (*weak formulation*), we introduce a combined parameterization consisting of finite elements and spherical harmonics that allows us to treat models with lateral variations of viscosity that span several orders of magnitude. In order to validate the SFE approach when LVV are considered, we derive a semi-analytical solution of the

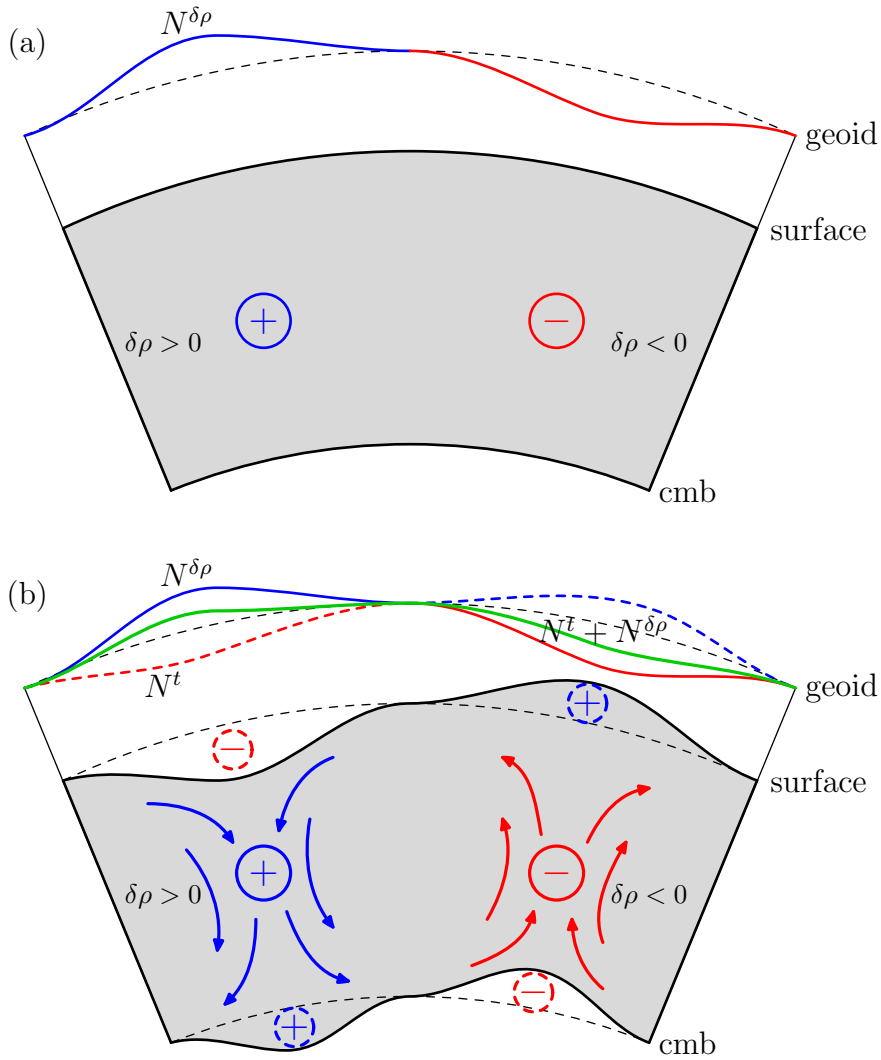

Figure 1: A cartoon illustrating the basic physical mechanism that explains the non-hydrostatic geoid. (a) Static geoid anomaly $N^{\delta\rho}$ due to the primary contribution of internal density anomalies $\delta\rho$: a positive (negative) geoid anomaly corresponds to a positive (negative) density anomaly. (b) Mantle flow associated with primary density anomalies causes boundary deformations and hence additional density anomalies, with which the geoid N^t (dashed line) is associated. The total geoid (green line) is the sum of the two contributions.

Stokes problem in the presence of a particular axisymmetric distribution of viscosity. Finally, the SFE method is applied to model the low-degree geoid associated with axisymmetric models of subduction.

1 Model equations and solution techniques

1.1 Equations and boundary conditions

On the global scale, mantle dynamics can be well approximated by modeling a selfgravitating Newtonian viscous incompressible fluid under the infinite Prandtl number approximation, i.e. with vanishing inertia (e.g. Hager & Clayton, 1989). For such a fluid, the mass conservation equation, the constitutive relation and the linear momentum equation read respectively as

$$\operatorname{div} \boldsymbol{u} = 0 \tag{1}$$

$$\boldsymbol{\tau} = -p\boldsymbol{I} + 2\eta\dot{\boldsymbol{\varepsilon}} \tag{2}$$

$$\operatorname{div} \boldsymbol{\tau} - \boldsymbol{g}_0\delta\rho + \rho_0 \operatorname{grad} V = 0 \tag{3}$$

where $\boldsymbol{u}$ is the Eulerian flow velocity, $\boldsymbol{\tau}$ is the Cauchy stress tensor, $\boldsymbol{I}$ is the identity tensor, $p \equiv \mathrm{Tr}(\boldsymbol{\tau})/3$ is the dynamic pressure (Tr is the trace operator), η is the shear viscosity, $\dot{\boldsymbol{\varepsilon}} \equiv (\operatorname{grad} \boldsymbol{u} + \operatorname{grad}{}^t\boldsymbol{u})/2$ is the strain-rate tensor, $\boldsymbol{g}_0\delta\rho$ is the buoyancy force that drives convection through lateral density heterogeneities $\delta\rho$, being $\boldsymbol{g}_0$ the reference gravity acceleration, ρ_0 is the reference density and V the gravitational potential that can be obtained by solving the Poisson equation with the anomalies $\delta\rho$ as source term:

$$\nabla^2 V = 4\pi G\delta\rho, \tag{4}$$

where G is the constant of gravitation.

Equations (1), (3) and (4) are to be satisfied within the mantle volume, which we will indicate by $\mathcal{B}$. On the boundary $\partial\mathcal{B} = \partial\mathcal{B}^{\mathrm{a}} \cup \partial\mathcal{B}^{\mathrm{c}}$, where $\partial\mathcal{B}^{\mathrm{a}}$ and $\partial\mathcal{B}^{\mathrm{c}}$ denote the Earth's surface and the core-mantle boundary, respectively, suitable boundary conditions must be specified. Equations (1) and (3) are typically solved by considering *fixed, impermeable and free-slip* boundaries (e.g. Thoraval et al., 1994), as follows:

$$\boldsymbol{u} \cdot \boldsymbol{e}_r = 0, \tag{5}$$

$$\boldsymbol{\tau} \cdot \boldsymbol{e}_r - ((\boldsymbol{\tau} \cdot \boldsymbol{e}_r) \cdot \boldsymbol{e}_r)\boldsymbol{e}_r = 0, \tag{6}$$

where $\boldsymbol{e}_r$ is the radial unit vector of a spherical reference system. The impermeability condition (5), guarantees that there is no mass flux across $\partial\mathcal{B}$, which is then fixed, while condition (6) requires the shear stresses to vanish on $\partial\mathcal{B}$. The normal component of the surface traction $\tau_{rr} = (\boldsymbol{\tau} \cdot \boldsymbol{e}_r) \cdot \boldsymbol{e}_r$ does not need to be zero. This is rather interpreted like the force that produces the *dynamic topography* h of the boundary $\partial\mathcal{B}$:

$$h = -\frac{\tau_{rr}}{\Delta\rho_0\, g_0}, \tag{7}$$

where $\Delta\rho_0$ is the change in the reference density across $\partial\mathcal{B}$ and g_0 the reference gravitational acceleration at $\partial\mathcal{B}$. Equation (7) has a clear physical meaning: The surface traction τ_{rr} balances the pressure force due to the displaced topography h.

The Poisson equation (4) is not valid at points where the density is discontinuous and in the presence of surface-mass density contrasts. Thus, it must be supplemented by suitable boundary conditions. In eq. (7), the dynamic topography h is small compared to the characteristic dimensions of the mantle. Therefore, we can define a surface-mass density contrast induced by mantle flow at the boundary $\partial\mathcal{B}$ as

$$\sigma^h \equiv h\,\Delta\rho_0 = -\frac{\tau_{rr}}{g_0}. \tag{8}$$

It can be shown (Dahlen, 1974) that, to account for density discontinuities and surface-mass density contrasts, respectively, at $\partial\mathcal{B}$, the gravitational potential and gravitational intensity must satisfy the following conditions:

$$[V]^+_- = 0, \tag{9}$$

$$[\boldsymbol{e}_r \cdot \operatorname{grad} V]^+_- + 4\pi G\sigma^h = 0, \tag{10}$$

where the symbol $[\bullet]^+_-$ indicates the jump of the quantity between brackets on $\partial\mathcal{B}$ and the super(sub)script $+$ $(-)$ denotes the evaluation of such a quantity on the external (internal) side of $\partial\mathcal{B}$.

Note that, in order to apply eqs (9) and (10), it is necessary to know the external potentials V^{a^+} and V^{c^-}, above the Earth's surface and beneath the CMB, respectively. In these regions there are no density anomalies (i.e., $\delta\rho$=0) and V simply satisfies the Laplace equation:

$$\nabla^2 V = 0. \tag{11}$$

The solution to eq. (11) can be expressed in terms of a spherical harmonic series. For a radius r larger than the Earth radius a, the potential reads as

$$V^{\mathrm{a}^+}(r,\Omega) = \sum_{jm} V^{\mathrm{a}^+}_{jm} \left(\frac{a}{r}\right)^{j+1} Y_{jm}(\Omega), \tag{12}$$

while at a radius smaller than the CMB radius c, we have

$$V^{\mathrm{c}^-}(r,\Omega) = \sum_{jm} V^{\mathrm{c}^-}_{jm} \left(\frac{r}{c}\right)^{j} Y_{jm}(\Omega), \tag{13}$$

where the symbol Ω is used to denote the angular variables (ϑ,φ).

1.2 Matrix propagator technique

In the presence of radially symmetric viscosity distributions, the matrix propagator technique (e.g. Gantmacher, 1990) allows us to construct an analytical solution to the boundary-value problem (1)–(9). After expanding the field variables into spherical harmonic functions, the PDE (1)–(4) are converted to a system of ordinary differential equations (ODE) for each degree and order of the spherical harmonic expansion.

The flow vector $\boldsymbol{u}$ and the traction vector $\boldsymbol{T} \equiv \boldsymbol{\tau} \cdot \boldsymbol{e}_r$ are expanded into vector spherical harmonics $\boldsymbol{S}_{jm}^{(\ell)}(\Omega)$, $\ell = -1, 0, 1$ (Phynney & Burridge, 1973):

$$\boldsymbol{u} = \sum_{jm} (u_{jm} \boldsymbol{S}_{jm}^{(-1)} + v_{jm} \boldsymbol{S}_{jm}^{(1)} + w_{jm} \boldsymbol{S}_{jm}^{(0)}), \tag{14}$$

$$\boldsymbol{T} = \sum_{jm} (\tau_{rr,jm} \boldsymbol{S}_{jm}^{(-1)} + \tau_{r\vartheta,jm} \boldsymbol{S}_{jm}^{(1)} + \tau_{r\varphi,jm} \boldsymbol{S}_{jm}^{(0)}), \tag{15}$$

where u_{jm} and v_{jm} are the spheroidal components and w_{jm} the toroidal component of $\boldsymbol{u}$. Similarly, the potential V and density anomalies $\delta\rho$ are expanded into scalar spherical harmonics (Varshalovich et al., 1989)

$$V = \sum_{jm} V_{jm} Y_{jm}, \tag{16}$$

$$\delta\rho = \sum_{jm} \delta\rho_{jm} Y_{jm}. \tag{17}$$

By transforming eqs (1)–(4) into spherical coordinates (Landau & Lifshitz, 1987) and using the expansions (14)–(17), two decoupled systems of ODE are obtained for toroidal and spheroidal variables respectively. On the one hand, as far as the first are concerned, we have

$$\frac{d\boldsymbol{y}_{\mathrm{T}}}{dr} = \boldsymbol{B}\, \boldsymbol{y}_{\mathrm{T}}, \tag{18}$$

where $\boldsymbol{y}_{\mathrm{T}} \equiv \left[w_{jm}, \tau_{r\varphi,jm}\right]^t$ and $\boldsymbol{B} = \boldsymbol{B}(\eta, r)$ is a matrix (see Sec. 2.3 of the thesis). Since neither a toroidal forcing nor boundary conditions for toroidal flow are prescribed, the vector $\boldsymbol{y}_{\mathrm{T}}$ satisfies a homogeneous system with homogeneous boundary conditions for each j and m. Hence, it has only the trivial solution $\boldsymbol{y}_{\mathrm{T}} = 0$. On the other hand, as far as the spheroidal variables are concerned, we have

$$\frac{d\boldsymbol{y}}{dr} = \boldsymbol{A}\, \boldsymbol{y} + \boldsymbol{b}, \tag{19}$$

where $\boldsymbol{y} \equiv \left[u_{jm}, v_{jm}, \tau_{rr,jm}, \tau_{r\vartheta,jm}, rV_{jm}, r^2 dV_{jm}/dr\right]^t$, $\boldsymbol{A} = \boldsymbol{A}(\eta, r)$ is the matrix of the system (see Sec. 2.3 of the thesis) and $\boldsymbol{b}$ is the forcing vector:

$$\boldsymbol{b} = \left[0, 0, g_0 \delta\rho_{jm} r^2, 0, 0, 4\pi G \delta\rho_{jm} r^3\right]^t.$$

For each degree and order j and m, the system (19) is equivalent to eqs (1)-(4) (with the assumption that $\eta = \eta(r)$).

If the solution to eq. (19) is known at an initial radius r_0, the solution corresponding to any radius $r > r_0$, enclosing a shell in which the matrix $\boldsymbol{A}$ is constant, can be obtained (Gantmacher, 1990) through the *matrix propagator* $\boldsymbol{P}$ as follows:

$$\boldsymbol{y}(r) = \boldsymbol{P}(r, r_0)\boldsymbol{y}(r_0) + \sum_{i=1}^{N} \boldsymbol{P}(r, r_i)\boldsymbol{b}(r_i). \tag{20}$$

Here $\boldsymbol{y}(r_0)$ is a known starting vector, while $\boldsymbol{P}(r, r_0)$ is the matrix propagator (Gilbert & Backus, 1966):

$$\boldsymbol{P}(r, r_0) = \boldsymbol{M}(r)\boldsymbol{M}^{-1}(r_0),$$

where $\boldsymbol{M}(r)$ is the fundamental matrix of the homogeneous system associated with eq. (19) (i.e. with $\boldsymbol{b} = 0$). In eq. (20) the continuous volumetric density perturbations $\delta\rho_{jm}(r)$ are approximated by a series of N discrete sheets of surface-mass density $\delta\sigma_{jm}(r_i)$ located at fixed depths r_i. According to this, the load vector reads now as

$$\boldsymbol{b} = \left[0, 0, g_0\delta\sigma_{jm}(r_i)r_i, 0, 0, 4\pi G\delta\sigma_{jm}(r_i)r_i^2\right]^t.$$

Equation (20) is only valid within a layer where the propagator is constant. To account for radial changes of viscosity, and consequent changes in the propagator, the property of the propagator matrix is be used according to which solution vectors can be propagated through a series of different material layers by simply forming the product of individual layer matrices. Finally, taking into account the boundary conditions, it can be shown that the solution vector $\boldsymbol{y}$ at the surface has the following form

$$\boldsymbol{y}(a) = \left[0, u_{jm}(a), \tau_{rr,jm}(a), 0, V_{jm}(a), -(j+1)V_{jm}(a) + \frac{4\pi G a^2 \tau_{rr,jm}(a)}{g_0}\right]^t, \quad (21)$$

while, at the CMB we have:

$$\boldsymbol{y}(c) = \left[0, u_{jm}(c), \tau_{rr,jm}(c), 0, V_{jm}(c), jV_{jm}(c) + \frac{4\pi G a^2 \tau_{rr,jm}(c)}{g_0}\right]^t. \quad (22)$$

Using eq. (20) with the boundary vectors (21) and (22) leads to solving a system of six equations in the six unknowns $u_{jm}(a)$, $\tau_{rr,jm}(a)$, $V_{jm}(a)$, $u_{jm}(c)$, $\tau_{rr,jm}(c)$, $V_{jm}(c)$. With this procedure, the starting solution $\boldsymbol{y}(c)$ is fully specified and can be propagated, using eq. (20), to any additional radius.

1.3 Spectral–finite element approach

When mantle viscosity is not simply radially distributed but exhibits lateral variations, spherical harmonic modes are coupled and the matrix propagator solution for individual degrees and orders is no longer applicable. To treat lateral viscosity variations (LVV), we apply the finite element method to find the solution of the Stokes-Poisson problem. The problem is first reformulated in a weak sense. Then, the resulting integral equations are parameterized using spherical harmonics to discretize the angular coordinates and piecewise linear finite elements to discretize the radial coordinate. This is the reason why we term our method the *spectral–finite element* (SFE) approach.

Matyska (1996) showed that by choosing a suitable functional space $\mathcal{S}$, the solution to the Stokes-Poisson problem (1)–(4) subject to boundary conditions (5)–(10)

can be obtained by finding the set of variables $(\boldsymbol{u}, p, \lambda, V) \in \mathcal{S}$ such that, for any set of corresponding test functions $(\delta\boldsymbol{u}, \delta p, \delta\lambda, \delta V) \in \mathcal{S}$, the following variational equalities are satisfied:

$$\delta\mathscr{E}(\boldsymbol{u}, p, \lambda, V, \delta\boldsymbol{u}, \delta p, \delta\lambda, \delta V) = \delta\mathscr{F}(\delta\boldsymbol{u}), \tag{23a}$$

$$\delta\mathscr{G}(V, \lambda, \delta V, \delta\lambda) = \delta\mathscr{H}(\delta V), \tag{23b}$$

where $\lambda \equiv \tau_{rr}\big|_{\partial\mathcal{B}}$, $\delta\mathscr{E} = \delta\mathscr{E}_{\dot{\varepsilon}} + \delta\mathscr{E}_p + \delta\mathscr{E}_\lambda + \delta\mathscr{E}_{sg}$ and the individual functional variations read as

$$\delta\mathscr{E}_{\dot{\varepsilon}} \equiv 2\int_{\mathcal{B}} \eta(\dot{\boldsymbol{\varepsilon}} : \delta\dot{\boldsymbol{\varepsilon}}) dV, \tag{24}$$

$$\delta\mathscr{E}_p \equiv -\int_{\mathcal{B}} \operatorname{div}\boldsymbol{u}\, \delta p\, dV - \int_{\mathcal{B}} p \operatorname{div}\delta\boldsymbol{u}\, dV, \tag{25}$$

$$\delta\mathscr{E}_\lambda \equiv -\int_{\partial\mathcal{B}} \boldsymbol{e}_r \cdot \boldsymbol{u}\, \delta\lambda\, dS - \int_{\partial\mathcal{B}} \lambda\, \boldsymbol{e}_r \cdot \delta\boldsymbol{u}\, dS, \tag{26}$$

$$\delta\mathscr{E}_{sg} \equiv \int_{\mathcal{B}} \rho_0 \operatorname{grad} V \cdot \delta\boldsymbol{u}\, dV, \tag{27}$$

$$\delta\mathscr{F} \equiv \int_{\mathcal{B}} \delta\rho \boldsymbol{g}_0 \cdot \delta\boldsymbol{u}\, dV, \tag{28}$$

$$\begin{aligned}\delta\mathscr{G} \equiv &\int_{\mathcal{B}} \operatorname{grad} V \cdot \operatorname{grad}\delta V\, dV + \frac{4\pi G}{g_0}\int_{\partial\mathcal{B}} \lambda\, \delta V\, dS \\ &- \int_{\partial\mathcal{B}} \boldsymbol{e}_r \cdot \operatorname{grad} V^+\, \delta V\, dS,\end{aligned} \tag{29}$$

$$\delta\mathscr{H} \equiv 4\pi G \int_{\mathcal{B}} \delta\rho\, \delta V\, dV. \tag{30}$$

The dynamic pressure p and the variable λ are used as Lagrange multipliers to enforce incompressibility and to adjust the boundary conditions, respectively.

The variational equalities (23) are then discretized as follows. On the one hand, the angular part of the solution and of the corresponding test functions is expanded into spherical harmonics. On the other hand, piecewise linear finite elements are employed to parameterize the radial part of the flow $\boldsymbol{u}$ and of the gravitational potential V, while piecewise constant functions are used for the pressure p. In this way, from eq. (23), a discrete system of linear equations is obtained that, at each node of the radial discretization, is solved for each degree and order of the unknowns by preconditioned conjugate gradient technique (Barrett et al., 1994).

1.4 Validation with 1D viscosity distributions

With the SFE approach both models with radially symmetric and laterally dependent viscosity distributions can be handled. Nevertheless this numerical method needs first to be validated. This is the main reason why the matrix propagator technique was implemented. The SFE solution is benchmarked against the matrix

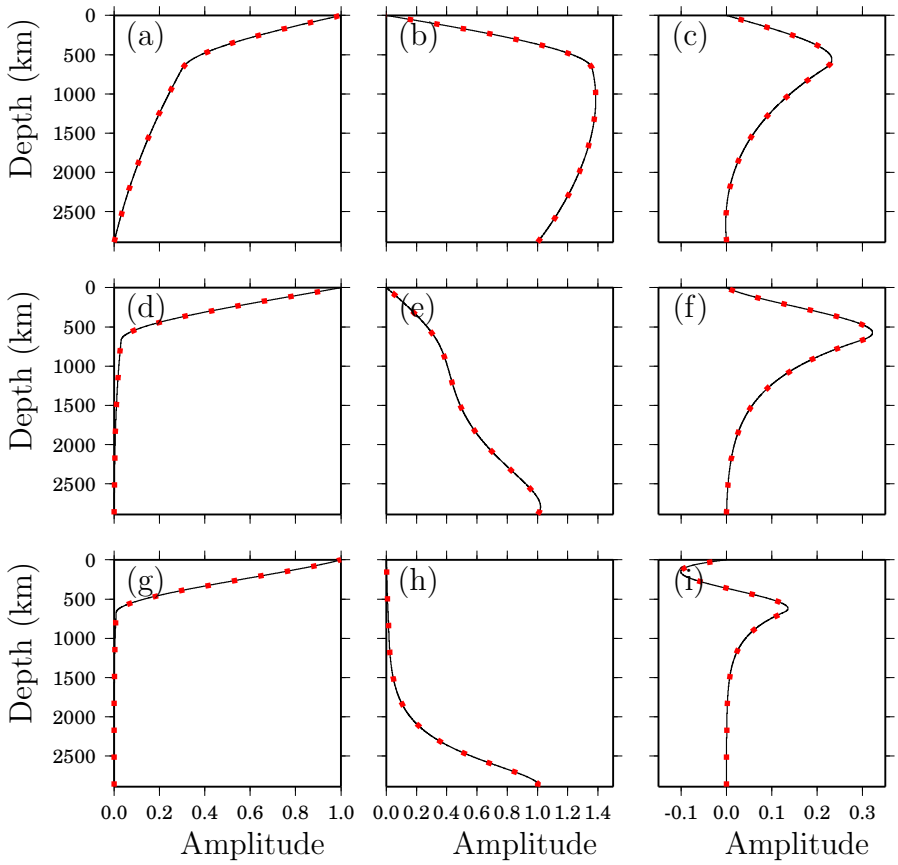

Figure 2: Matrix propagator solution (black lines) versus SFE solution (red squares) for a two-layer mantle. Green's functions of surface dynamic topography (panels a, d, g), CMB dynamic topography (panels b, e, h) and geoid (panels c, f, i) are plotted for degree $j = 2$ (panels a, b, c), $j = 8$ (panels d, e, f) and $j = 16$ (panels g, h, i).

propagator solution by comparing Green's functions for the geoid and dynamic topography (Corrieu et al., 1995) in the presence of stratified viscosity distributions. At several mantle depths, 'delta–like' unitary harmonic loads are prescribed and the resulting geoid, surface and CMB topographies are computed with the two methods. As example, Fig. 2 shows the comparison between the Green's functions for dynamic surface topography, CMB topography and geoid obtained via matrix propagator (black lines) and SFE technique (red squares) for a two–layers mantle, with the lower mantle being 100–times more viscous than the upper mantle ($\eta_{\rm lm}/\eta_{\rm um} = 100$) and load/response harmonic degrees $j = 2$, 8, 16. Surface and CMB topography kernels are normalized by their own value at the Earth's surface and at the CMB, respectively, while the geoid is normalized by the factor $4\pi Ga/(2j+1)g_0$. The agreement agreement between the two solutions is very good and the error is always found to be within 1%. In Fig. 2, the number of finite elements employed to plot the SFE solution is 80. Nevertheless, it is interesting to show how the SFE solution converges to the matrix propagator solution as the number of finite elements is increased. In Fig. 3, we show the convergency test for the geoid kernel of degree $j = 16$. The

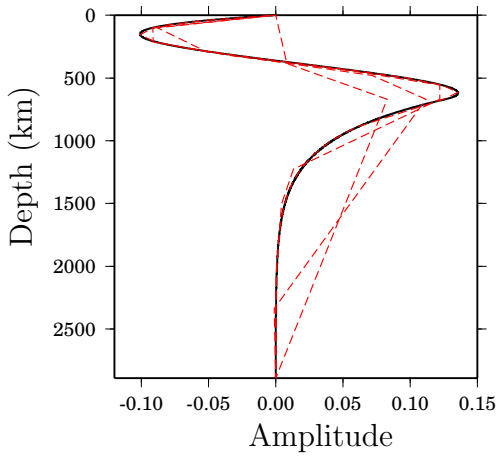

Figure 3: Convergency of the SFE solution (red dashed line) to the matrix propagator solution (black solid line) as the number N of finite elements is increased. The geoid Green's function of degree 16 with $\eta_{\rm lm}/\eta_{\rm um} = 100$ is shown. The SFE solution is plotted for N =5, 10, 20 and 60.

numerical solution converges quite rapidly to the analytical one. We start with 5 finite elements and increase their number up to 60 with which the two curves are practically indistinguishable.

2 A semi-analytical solution for axisymmetric viscosity

With the benchmark against the matrix propagator solution, the SFE approach has proven to be correct when radially symmetric viscosity distributions are considered. In order to validate our approach in the presence of LVV, we derived a semi-analytical solution for computing 2-D axisymmetric viscous Stokes flow in a model consisting of two eccentrically nested spheres (ENS) of different viscosities.

2.1 Outline of the solution

The construction of the ENS solution is rather technical. Here we present a short outline, referring the reader to Chapter 5 of the thesis for a more detailed derivation. For the special geometrical configuration shown in Fig. 4, we derive a solution to the Stokes equation (3) with the self-gravitation term neglected:

$$\operatorname{div} \boldsymbol{\tau} + \boldsymbol{f} = 0 \ \text{ in } \mathcal{S}, \tag{31}$$

where $\mathcal{S}$ is now a full sphere and $\boldsymbol{f}$ is a general forcing term expressing an internal load associated with lateral density anomalies. The flow is again considered as incompressible (see eq. 1) and the boundary $\partial\mathcal{S}$ of the sphere impermeable and free-slip (see eqs 5 and 6).

The first step of our derivation follows observing that the flow vector $\boldsymbol{u}$ can be decomposed as the sum of a spheroidal vector $\boldsymbol{u}_s$ and a toroidal vector $\boldsymbol{u}_t$ (e.g. Chandrasekhar, 1968)

$$\boldsymbol{u} = \boldsymbol{u}_s + \boldsymbol{u}_t. \tag{32}$$

Assuming that the viscosity η is axisymmetric, that is $\eta = \eta(r, \vartheta)$, and considering an internal forcing $\boldsymbol{f}$ with no toroidal component, which is consistent with the assumption of gravitational forcing, it can be shown that the linear momentum equation and the incompressibility condition can be written separately for $\boldsymbol{u}_s$ and $\boldsymbol{u}_t$ as follows:

$$-\operatorname{grad} p + \operatorname{grad} \eta \cdot (\operatorname{grad} \boldsymbol{u}_s + \operatorname{grad}{}^t \boldsymbol{u}_s) - \eta \operatorname{rot} \operatorname{rot} \boldsymbol{u}_s + \boldsymbol{f} = 0 \tag{33a}$$

$$\operatorname{div} \boldsymbol{u}_s = 0, \tag{33b}$$

and

$$\operatorname{grad} \eta \cdot (\operatorname{grad} \boldsymbol{u}_t + \operatorname{grad}{}^t \boldsymbol{u}_t) - \eta \operatorname{rot} \operatorname{rot} \boldsymbol{u}_t = 0 \tag{34a}$$

$$\operatorname{div} \boldsymbol{u}_t = 0. \tag{34b}$$

Since no surface toroidal forcing is prescribed, the homogeneous system of equations (34) is supplemented by homogeneous boundary conditions and thus it has only the trivial solution $\boldsymbol{u}_t = 0$. Therefore, we just deal with the system (33) for the spheroidal flow $\boldsymbol{u}_s$, which will be simply denoted by $\boldsymbol{u}$.

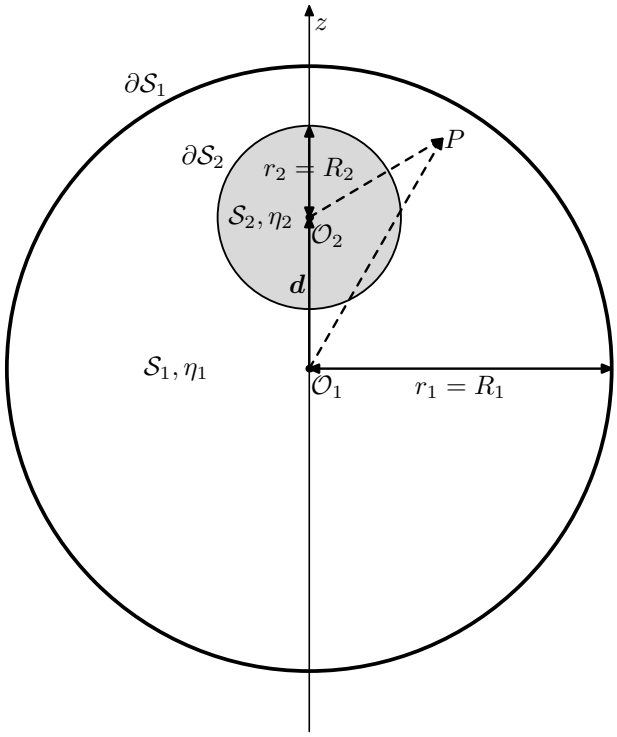

Figure 4: Geometry of the two eccentrically nested spheres. The outer sphere of radius R_1 and viscosity η_1 is centered at $\mathcal{O}_1$, representing the origin of a spherical coordinate system $\mathcal{O}_1(r_1, \vartheta_1)$. The grey sphere $\mathcal{S}_2$ of viscosity η_2 is centered at $\mathcal{O}_2$, representing the origin of a spherical coordinate system $\mathcal{O}_2(r_2, \vartheta_2)$ shifted by the vector $\boldsymbol{d}$ along the z-axis.

To solve the system of equations (33) in a sphere, a solution to eqs (33) is expressed as the sum of two parts: the solution to the *homogeneous* problem with $\boldsymbol{f} = 0$ and a *particular* solution with $\boldsymbol{f} \neq 0$:

$$p = p^0 + p', \tag{35}$$
$$\boldsymbol{u} = \boldsymbol{u}^0 + \boldsymbol{u}', \tag{36}$$

where the labels ^{0} and $'$ denote the homogeneous solution and a particular solution, respectively. By suitably choosing the particular solutions and accordingly the load $\boldsymbol{f}$, it can be shown that the system (33) can be reduced to the biharmonic differential equation for the toroidal vector potential $\boldsymbol{A}$ (implicitly defined by the relation $\boldsymbol{u}^0 = \text{rot}\,\boldsymbol{A}$):

$$\nabla^4 \boldsymbol{A} = 0. \tag{37}$$

The fact that toroidal vector spherical harmonics $\boldsymbol{S}^{(0)}_{jm}$ are eigenfunctions of the Laplace operator, i.e. $[\nabla^2 + j(j+1)]\boldsymbol{S}^{(0)}_{jm} = 0$, is used to show that the fundamental solution to eq. (37) can be written as

$$\boldsymbol{A}(r, \vartheta) = \sum_j (A_{1,j} r^j + A_{2,j} r^{j+2} + A_{3,j} r^{-j-1} + A_{4,j} r^{-j+1}) \boldsymbol{S}^{(0)}_j(\vartheta), \tag{38}$$

where $A_{i,j}$, $i = 1, \ldots, 4$ are constant of integrations to be determined from the boundary conditions.

In Fig. 4, a large sphere $\mathcal{S}_1$ contains a smaller sphere $\mathcal{S}_2$. Since the solution (38) is valid for a homogeneous sphere, it can be used to write the solutions for the outer and inner spheres separately. In the reference frame of $\mathcal{S}_2$, we then have

$$\boldsymbol{A}^{(1)}(r_2, \vartheta_2) = \sum_j (A_{3,j} r_2^j + A_{4,j} r_2^{j+2} + A_{5,j} r_2^{-j-1} + A_{6,j} r_2^{-j+1}) \boldsymbol{S}_j^{(0)}(\vartheta_2), \qquad (39)$$

where the dependence on r_2 and ϑ_2 is written explicitely to emphasize that the solution is expressed in the coordinate system $\mathcal{O}_2$. On the other hand, the toroidal vector potential inside $\mathcal{S}_2$ is

$$\boldsymbol{A}^{(2)}(r_2, \vartheta_2) = \sum_j (A_{1,j} r_2^j + A_{2,j} r_2^{j+2}) \boldsymbol{S}_j^{(0)}(\vartheta_2). \qquad (40)$$

Note that the expression (40) does not contain the harmonics $r_2^{-j-1}\boldsymbol{S}_j^{(0)}$ and $r_2^{-j+1}\boldsymbol{S}_j^{(0)}$ because they are singular at the origin $\mathcal{O}_2$ where $r_2 \to 0$. The solution to our original problem is then found once, for each degree j, the six constants of integration $A_{i,j}$, $i = 1, \ldots, 6$ are known. Four such constants are determined by connecting continuously flow and stresses at the interface $r_2 = R_2$, i.e.:

$$u_j^{(1)}(r_2 = R_2) = u_j^{(2)}(r_2 = R_2) \quad \text{and} \quad v_j^{(1)}(r_2 = R_2) = v_j^{(2)}(r_2 = R_2)$$
$$\tau_{rr,j}^{(1)}(r_2 = R_2) = \tau_{rr,j}^{(2)}(r_2 = R_2) \quad \text{and} \quad \tau_{r\vartheta,j}^{(1)}(r_2 = R_2) = \tau_{r\vartheta,j}^{(2)}(r_2 = R_2),$$

while the remaining two constants are obtained by imposing the impermeability and free-slip conditions at $r_1 = R_1$, i.e.:

$$u_j^{(1)}(r_1 = R_1) = 0 \quad \text{and} \quad \tau_{r\vartheta,j}^{(1)}(r_1 = R_1) = 0.$$

Note that since the latter two conditions are expressed in the reference system $\mathcal{O}_1$, the potential $\boldsymbol{A}^{(1)}(r_2, \vartheta_2)$ needs to be transformed to $\boldsymbol{A}^{(1)}(r_1, \vartheta_1)$. This can be accomplished by applying suitable transformation theorems that permit to translate spherical harmonic functions employing particular combinations of the Clebsch-Gordan coefficients (Tosi & Martinec, 2007).

2.2 Comparison with the SFE solution

Several test examples are considered to compare the SFE and ENS solutions. In Fig. 5 the comparison is shown for an inner sphere 2000-times more viscous than the outer sphere. The cut-off degree of the spherical harmonic expansions of the SFE solution is 40 and the number of radial finite-elements employed 500. In all the examples considered, the agreement between the two solutions is always satisfactory.

The accuracy of the SFE solution can be improved by increasing the number of finite elements and/or the cut-off degree of the spherical harmonic expansion. For specific angular and radial cross-sections, we show in Fig. 6 the Root Mean Square

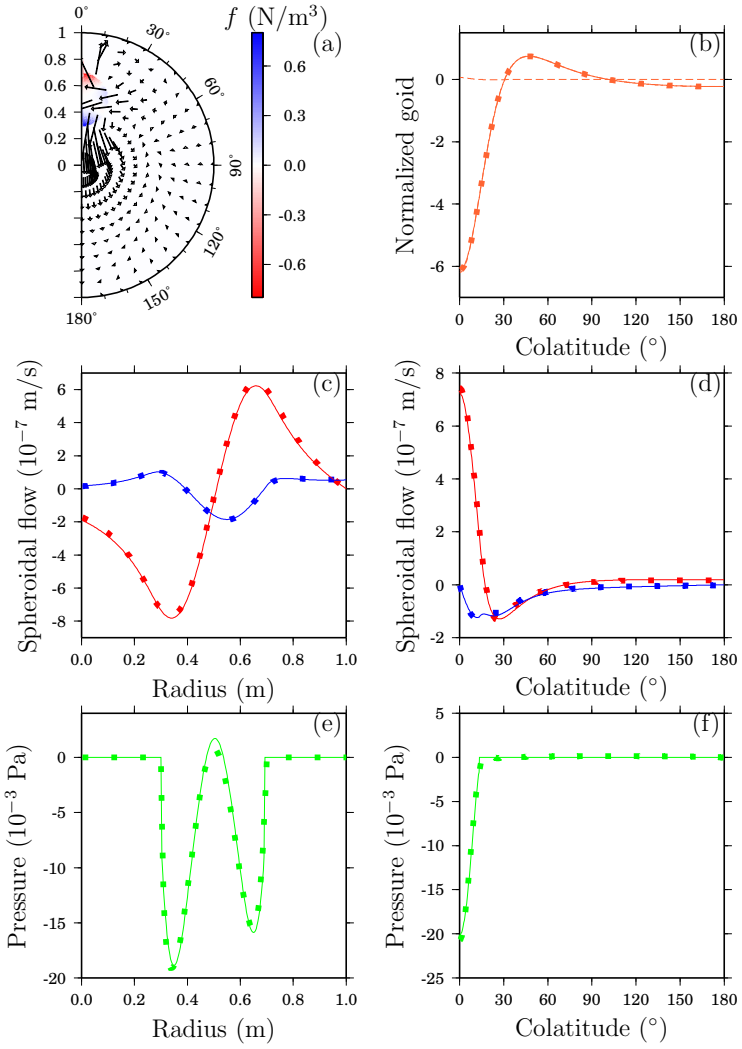

Figure 5: Comparison between SFE (squares) and ENS (solid line) solutions. Panel a: Flow pattern and density anomaly; panel b: Total geoid (solid line for ENS and squares for SFE), geoid due to internal anomaly (dashed-dotted line) and to boundary deformation (dashed line); panel c: Radial cross sections for radial flow (in red) and tangential flow (in blue); panel d: Angular cross section for for radial flow (in red) and tangential flow (in blue); panel e: Radial cross section for pressure; panel d: Angular cross section for pressure.

(RMS) error reduction for flow and pressure in models with increasing viscosity contrast between the inner and outer sphere. Because of the different functional space chosen to discretize the pressure (piecewise constant instead of piecewise linear functions are used), it is not surprising that this variable exhibits a lager error than that found for the flow. As expected, the RMS error increases along with the viscosity contrast.

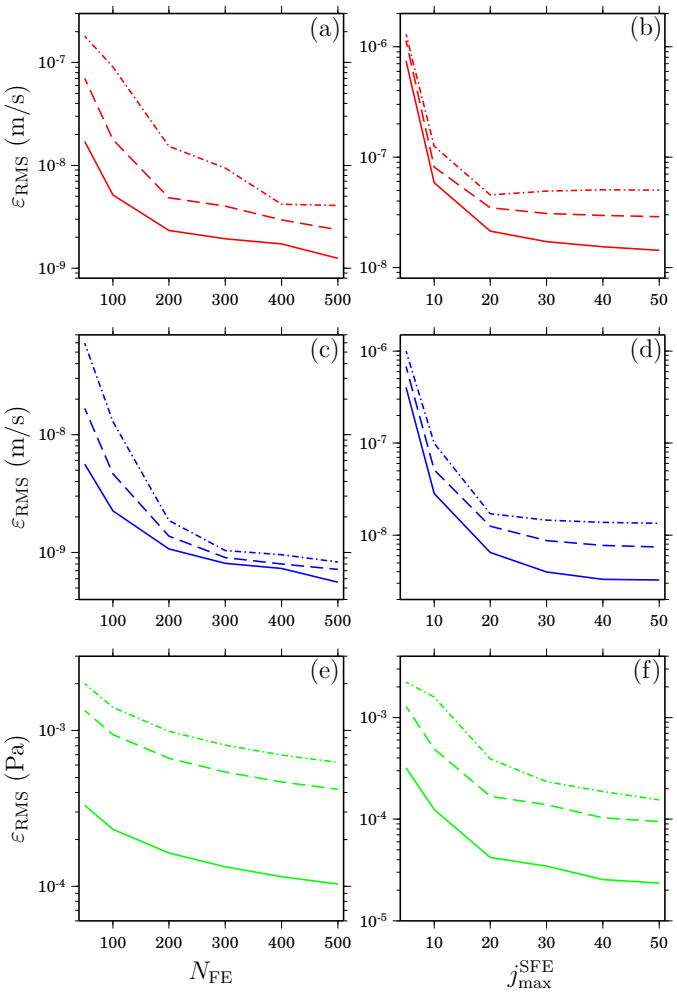

Figure 6: RMS error reduction for radial (panels a, c and e) and angular (panels b, d and f) cross sections for radial flow (red), tangential flow (blue) and pressure (green). Solid, dashed and dashed-dotted lines indicate models where the inner sphere is 50-, 200- and 2000-times more viscous than the outer sphere.

3 Low-degree geoid over subduction zones

Using the SFE approach, we perform numerical experiments to investigate in a spherical axisymmetric geometry the effects of LVV on the low-degree geoid and gravity anomalies over a typical subduction zone. We explore the parameters space, testing several combinations of density, viscosity and geometry of a subducted slab having a realistic lateral extent ($\sim$ 100 km), with the aim of predicting the characteristic broad positive highs that the low-degree geoid and gravity anomalies exhibit over major subduction zones.

3.1 Model setting

At long-wavelengths ($2 \leq j \leq 8$), geoid and gravity anomalies generally exhibit local maxima over convergent plate margins. For example, broad geoid maxima up to 60 degrees wide range from slightly more than 20 m over the subduction zones of South America and Japan up to 40 and 60 m over the Tonga and New Guinea regions, respectively, while the amplitude of the highs of gravity anomalies ranges between 15 and 25 mgal. To study such signals, we use a spherical axisymmetric mantle model. We consider a model consisting of three viscosity layers: lithosphere ($\eta_{\rm lith}$) extending from the Earth's surface to 100 km depth, upper mantle ($\eta_{\rm um}$) from the base of the lithosphere to 670 km depth and lower mantle ($\eta_{\rm lm}$) from the base of the upper mantle to the core-mantle boundary. The viscosity of the upper mantle is kept fixed at the reference value of $\eta_{\rm um} = 10^{20}$ Pa s. At colatitude $\vartheta = 80°$, we locate the trench where an oceanic plate subducts at a constant dip angle of 50°. The thickness of the subducting plate is 100 km everywhere. In those models that incorporate LVV, the viscosity of the slab ($\eta_{\rm slab}$) equals that of the lithosphere at every depth. Figure 7 shows as an example 2D axisymmetric viscosity structure.

The model is loaded using four buoyancy structures that differ from each other according to the depth of penetration of the slab as follows: (a) the slab is confined in the upper mantle, (b) the slab reaches the middle lower mantle, (c) the slab reaches the CMB, (d) the slab reaches the CMB and thickens in the lower mantle. For each such density structures, several radially symmetric and axisymmetric configurations of viscosity are tested and the resulting geoid and gravity anomalies are computed.

3.2 Results and discussion

The main goal of our analysis is to investigate which mantle models are able to produce broad positive geoid and gravity anomalies over the subducting plate and, at the same time, to assess the role played by LVV.

The first important result we obtained, that also confirms the conclusions emerging from other studies (e.g. Hager & Clayton, 1989; Corrieu et al., 1995), is that the viscosity ratio $\eta_{\rm lm}/\eta_{\rm um}$ is responsible for first-order effects and is crucial to obtain the correct sign for the geoid and gravity anomalies. In fact, independently of the buoyancy structure used and of the presence of LVV, all models where $\eta_{\rm lm}$ is less than 50-times larger than $\eta_{\rm um}$ present negative geoid and gravity anomalies that are

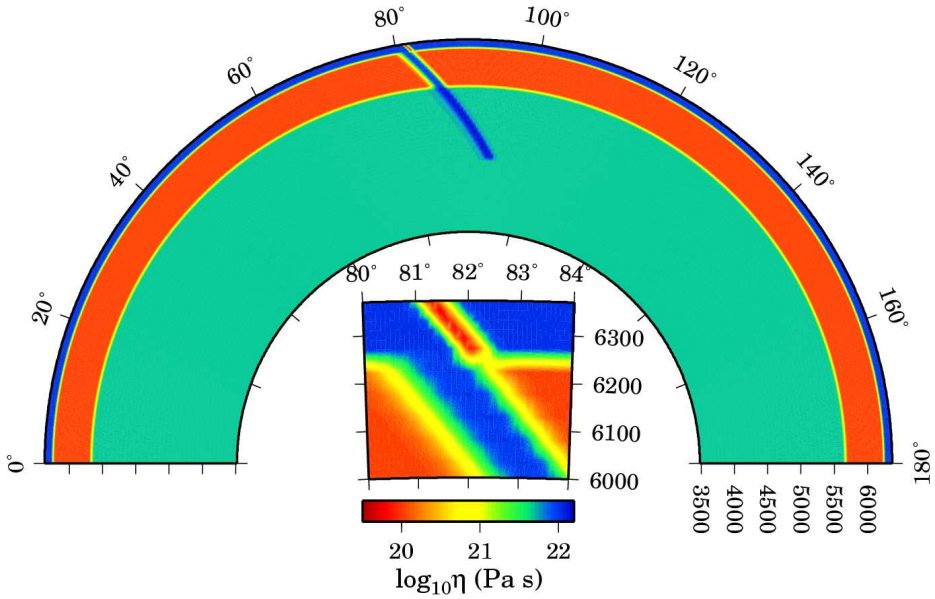

Figure 7: Typical viscosity structure. Here, a 2D viscosity model is shown for a slab extending to the middle lower mantle (density model 'd') along with a zoom on the trench region where a low viscosity zone is used to decouple the plates.

not compatible with the observations (Fig. 8). On the contrary, when $\eta_{\rm lm} \geq 50\,\eta_{\rm um}$, independently again of the buoyancy structure used and of the presence of LVV, the geoid and gravity induced by the slab are always characterized by broad highs, with several viscosity configurations ensuring realistic amplitudes that are comparable with the observations (Fig. 9)

Looking at Fig. 9, two further conclusions emerge. First, as far as the density structure is concerned, we found that if the slab is confined in the upper mantle (density models 'a'), the peaks in the geoid and gravity are always extremely small. Even though our models are not able to furnish indications about the depth that a slab should reach to ensure a good signal in the long-wavelength gravity field, they strongly suggest the need for the presence of well defined density anomalies in the lower mantle. It seems then necessary that at least a portion of the slab penetrates the 660 km discontinuity. Second, concerning the role of LVV, the largest differences between 1D and 2D viscosity distributions arise in those models for which the slab is confined in the upper mantle (density models 'a'). Using LVV in the slab region approximately doubles the moderate highs that appear over the subduction zone when a 1D viscosity model is employed. However, this is not the case for the other density models. When models 'b', 'c' or 'd' are used, the differences in amplitudes of the geoid or gravity anomalies between 1D and 2D viscosity models are definitely minor, though they tend to increase as the slab is assigned more excess mass. Interestingly, the most evident effect caused by the introduction of LVV into the models is to systematically shift the geoid and gravity profiles towards the trench region in an inversely proportional manner to the slab degree of buoyancy. On the one hand, profiles arising from 1D viscosity models all exhibit their maxima

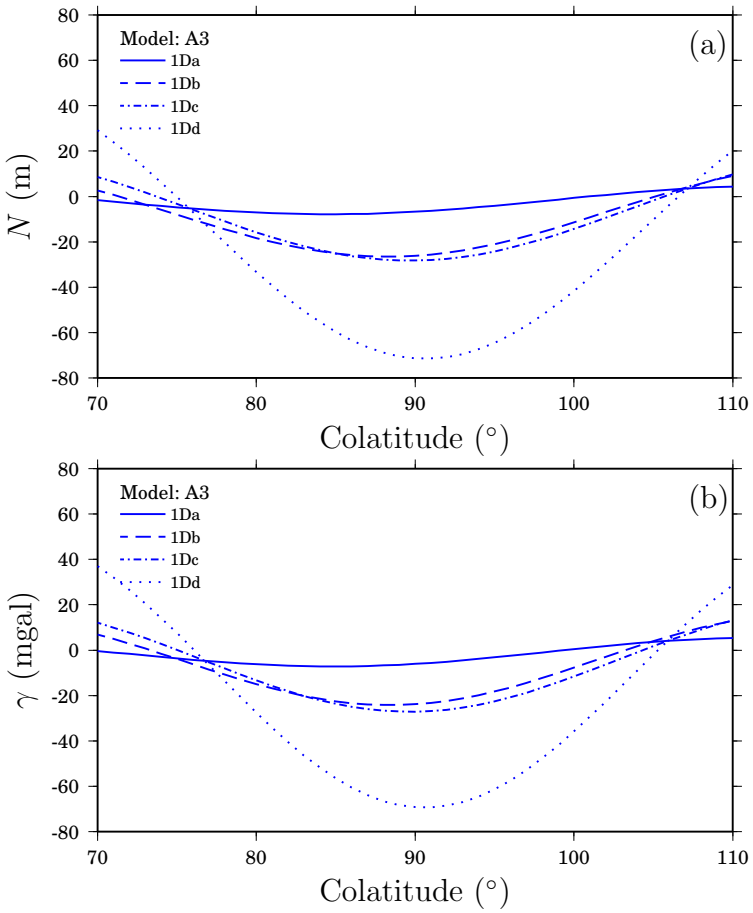

Figure 8: Geoid (a) and gravity anomaly (b) for a 1D viscosity model with $\eta_{\text{lith}} = 5 \cdot 10^{21}$ Pa s and $\eta_{\text{lm}} = 5 \cdot 10^{20}$ Pa s. Density models 'a', 'b', 'c' and 'd' are specified according to the line style indicated in the legend. For all density structures geoid and gravity are negative over the subduction zone.

approximately at 90° colatitude, i.e. 10° away of the trench. However, for 2D viscosity models, the high viscosity assigned to the slab is able to better focus the internal loading, with profiles obtained taking LVV into account having maxima directly above the trench for 'a' models and progressively away from it for models 'b', 'c' and 'd'. The differences between results obtained using 1D and 2D viscosity models are clearly minor and seem to indicate that, at least in the lower mantle, the presence of stiff slabs is not necessary when a fit to the long-wavelength slab geoid is sought.

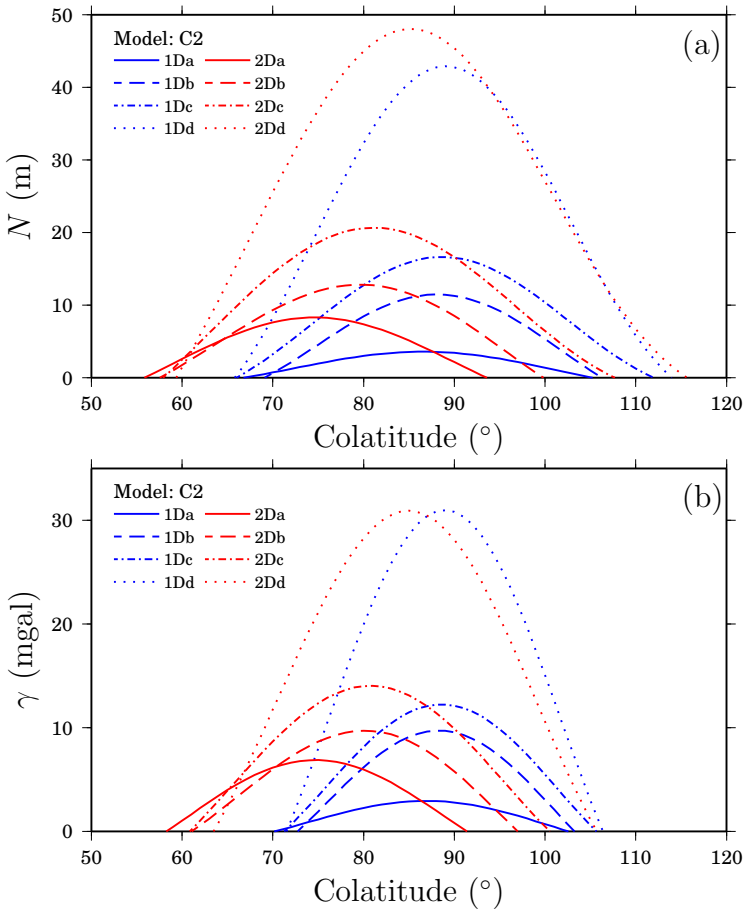

Figure 9: As in Fig. 8 but with $\eta_{\mathrm{lith/slab}} = 10^{22}$ Pa s and $\eta_{\mathrm{lm}} = 5 \cdot 10^{21}$ Pa s. Blue and red lines refer here to 1D and 2D viscosity distributions, respectively.

Conclusions

The main goal of this work has been the development of a reliable and efficient numerical model for the solution of the present-day mantle convection problem. We have implemented a solution scheme based on a weak formulation of the coupled Stokes-Poisson problem. Although the finite element method is nowadays a standard tool in geodynamics research, here it was used for the first time in combination with a spectral parameterization based on spherical harmonics to treat viscous flow models in a spherical geometry.

The classical technique based on propagator matrices provides us with an analytical solution of the Stokes-Poisson problem in the presence of laterally homogeneous viscosity distributions. This has been derived and implemented in order to validate the spectral finite element (SFE) method. The SFE and matrix propagator solutions have been compared using Green's functions obtained from simple internal loads and a satisfactory agreement was always achieved.

The SFE method is designed to treat lateral viscosity variations (LVV). The lack of well documented benchmark tests in the presence of LVV motivated us to derive and implement a semi-analytical solution of the Stokes problem for a special configuration consisting of two viscous eccentrically nested spheres (ENS). After careful testing, evidence has been provided that the semi-analytical solution is correct, and that our numerical code is accurate in solving problems with 2D viscosity distributions.

An axisymmetric viscosity model has been used to investigate the low-degree geoid signal induced by a typical subduction, with the aim of predicting the characteristic broad highs observed over major subduction zones and estimating the role played by very localized LVV. Several high resolution density and viscosity models have been systematically analyzed. On the one hand, our case study has confirmed that the viscosity contrast between upper and lower mantle is responsible for the first order effects on geoid predictions. A lower mantle at least one order of magnitude more viscous than the upper mantle is necessary to ensure a positive geoid signal of realistic amplitude. On the other hand, LVV are not able to modify significantly the amplitude of the low-degree geoid, suggesting then no need to consider stiff slabs while modeling the long-wavelength geoid.

Unfortunately, although fully 3D viscosity models can be handled with our SFE method, their demands in terms of computational power, along with the lack of adequate hardware, made it not feasible to present here meaningful examples derived from them.

References

Barrett, R., Berry, M., Chan, T., Demmel, J., Donato, J., Dongarra, J., Eijkhout, V., Pozo, R., Romine, C., & Van der Vorst, H., 1994, *Templates for the solution of linear systems: Building blocks for iterative methods, 2nd Edition*, SIAM, Philadelphia, PA.

Chandrasekhar, S., 1968, *Hydrodynamic and hydromagnetic stability*, The international series of monographs on physics, Clarendon Press, Oxford.

Corrieu, V., Thoraval, C., & Ricard, Y., 1995, Mantle dynamics and geoid Green functions, *Geophys. J. Int.*, **120**, 516–523.

Dahlen, F., 1974, On the static deformation of an Earth model with a fluid core, *Geophys, J. R. astr. Soc.*, **36**, 461–485.

Gantmacher, F., 1990, *Matrix theory*, American Mathematical Society, 2nd edn.

Gilbert, F. & Backus, G. E., 1966, Propagator matrices in elastic wave and vibration problems, *Geophys.*, **31**(2), 326–332.

Hager, B. H. & Clayton, R., 1989, Constraints on the structure of mantle convection using seismic observations, flow models, and the geoid, in *Mantle Convection, Plate Tectonics and Global Dynamics*, edited by W. Peltier, pp. 657–763, Gordon and Breach, Newark, N.J.

Landau, L. & Lifshitz, E., 1987, *Fluid mechanics*, vol. 6 of Course of theoretical physics, Butterworth Heinemann, Oxford, 2nd edn.

Matyska, C., 1996, Variational principles for the momentum equation of mantle convection with Newtonian and power-law rheologies, *Geophys. J. Int.*, **126**, 281–286.

Pekeris, C. L., 1935, Thermal convection in the interior of the Earth, *Mont. Not. R. Astron. Soc. Geophys. Suppl.*, pp. 343–367.

Phynney, R. & Burridge, R., 1973, Representation of elastic-gravitational excitation of a spherical Earth model by generalized spherical harmonics, *Geophys, J. R. astr. Soc.*, **34**, 451–487.

Ricard, Y., Fleitout, L., & Froidevaux, C., 1984, Geoid heights and lithospheric stresses for a dynamic Earth, *Ann. Geophys.*, **2**(3), 267–286.

Ritsema, J. & van Heijst, H. J., 2000, Seismic imaging of structural heterogeneity in Earth's mantle: Evidence for large scale mantle flow, *Sci. Progr.*, **93**, 243–259.

Runcorn, S., 1967, Flow in the mantle inferred from low degree harmonics of the geopotential, *Geophys. J. R. astr. Soc.*, **14**, 375–384.

Thoraval, C., Machetel, P., & Cazenave, A., 1994, Influence of mantle compressibility and ocean warping on dynamical models of geoid, *Geophys. J. Int.*, **117**, 566–573.

Tosi, N. & Martinec, Z., 2007, Semi-analytical solution for viscous Stokes flow in two eccentrically nested spheres, *Geophys. J. Int.*, pp. 1–16, 10.1111/j.1365-246X.2007.03482.x.

van der Hilst, R., Widiyantoro, S., & Engdahl, E., 1997, Evidence of deep mantle circulation from global tomography, *Nature*, **386**, 578–584.

Varshalovich, D., Moskalev, A., & Khersonskii, V., 1989, *Quantum theory of angular momentum*, World Scientific Publ., Singapore.